

Quantitative diffuse optical tomography for small animals using an ultrafast gated image intensifier

Sachin V. Patwardhan

Joseph P. Culver

Washington University School of Medicine
Department of Radiology
Mallinckrodt Institute of Radiology
St. Louis, Missouri 63110

Abstract. The quantitative accuracy of fluorescence and bioluminescence imaging of small animals can be improved by knowledge of the *in situ* optical properties of each animal. Obtaining *in situ* optical property maps is challenging, however, due to short propagation distances, requirements for high dynamic range, and the need for dense spatial, temporal, and spectral sampling. Using an ultrafast gated image intensifier and a pulsed laser source, we have developed a small animal diffuse optical tomography system with multiple synthetic modulation frequencies up to >1 GHz. We show that amplitude and phase measurements with useful contrast-to-noise ratios can be obtained for modulation frequencies over the range of ~ 250 to 1250 MHz. Experiments with tissue simulating phantoms demonstrate the feasibility of reconstructing the absorption and scattering optical properties in a small animal imaging system. © 2008 Society of Photo-Optical Instrumentation Engineers. [DOI: 10.1117/1.2830656]

Keywords: small animal imaging; diffuse optical tomography; fluorescence imaging; molecular imaging; near-infrared (NIR) spectroscopy.

Paper 06363RR received Dec. 12, 2006; revised manuscript received Aug. 30, 2007; accepted for publication Sep. 4, 2007; published online Feb. 29, 2008.

1 Introduction

Optical approaches to small animal *in vivo* molecular imaging provide high sensitivity, stable nonradioactive probes, and an extensive array of functional reporting strategies. However, quantitative whole body assays remain elusive. While planar fluorescence reflectance imagers (FRI) provide quick assessment of probe concentrations, quantitative localization is lacking due to a rapid decrease in sensitivity with increased depth, masking of buried targets by superficial tissues, and poor resolution. Recently, the feasibility of *in vivo* continuous-wave fluorescence tomography (CWFT) has been demonstrated in small animals.^{1,2} CWFT addresses some of the limitations of FRI and can provide even sensitivity versus depth throughout live, intact mice.

A critical aspect of fluorescence tomography has been the use of differential measurements, often a ratio of the fluorescence emission intensity over the reemitted excitation light intensity.³ Emission/excitation ratio measurements reduce the influence of heterogeneous optical properties and path lengths.⁴ Thus far, small animal fluorescence tomography studies have therefore generally assumed homogeneous optical properties for image reconstruction.^{1,2} Previous studies that examined the influence of heterogeneous optical properties upon linear reconstructions of ratio metric data have come to different conclusions. Some studies have found the influence of moderately absorbing backgrounds on linear reconstructions to be weak,^{4,5} while other studies have found a more significant effect.^{6,7} The different conclusions are due in

large part to differences in the optical property scenarios evaluated. For our application interest—whole body mouse imaging—it is reasonable to expect optical properties in mice to vary by an order of magnitude. Given these variations in optical properties, the incorrect assumption of homogeneous tissue properties can create significant errors in the reconstructed fluorescence concentrations.

Obtaining *in situ* optical properties is challenging. Monochromatic CW data is ill-suited for separation of absorption and scattering optical properties,⁸ which has motivated temporally resolved measurement approaches, either with frequency-domain⁹ or time-domain modulation.^{10,11} To take advantage of high-density spatial sampling and to achieve good temporal resolution, gated image intensified charge coupled devices (GICCD) have been used with both frequency-domain¹² and time-domain^{13,14} approaches. However, the use of GICCD tomography systems with time resolution above 300 MHz has focused primarily on imaging fluorescence lifetimes,¹² using early time gates for increased spatial resolution¹⁴ or late time gates for increased depth penetration.¹³ Time-resolved measurements for independent volumetric maps of absorption and scattering have generally been limited to large tissue volumes^{9,12} and modulation frequencies of <300 MHz. For small animal measurements with short source-detector separations, the measured pulse delays will be small, suggesting that the use of higher-modulation frequencies might be beneficial. High frequencies can offer better contrast between scattering and absorbing objects and higher resolution.¹⁵ Further, multiple modulation frequencies can separate absorption and scattering coefficients at a single, fixed source-detector separation.¹⁶

Address all correspondence to Joseph P. Culver, Washington University School of Medicine, Department of Radiology, Mallinckrodt Institute of Radiology, 4525 Scott Avenue—East Building, #1137, Campus Box #8225, St. Louis, Missouri 63110. Tel: 314-747-1341; Fax: 314-747-5191; E-mail: culverj@wustl.edu

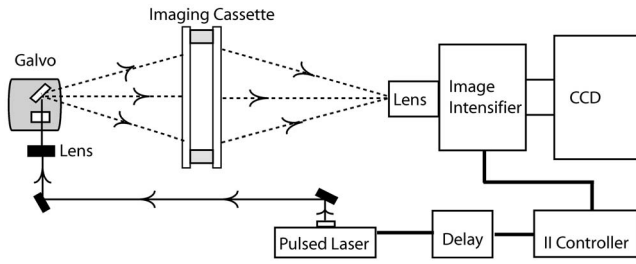


Fig. 1 Schematic of a TD-DOT system for small animal imaging: A pulsed laser source beam ($T_p=100$ ps) passes through the focusing lens and is steered by pair of galvanometer scanning mirrors to the source side of an imaging cassette. Light emitted from the detector plane of the imaging cassette is filtered and collected by a lens and temporally gated by a gated image intensifier. The temporally gated image is relayed to a CCD camera for readout. Timing between the source laser trigger signal and the gated detection is controlled by a programmable delay unit.

We present herein a time-resolved, ICCD-based small animal tomography system for obtaining quantitative absorption and scattering optical property maps. Using Fourier-transformed time-domain data, we show that measurements with useful contrast-to-noise ratios can be obtained even for modulation frequencies >1 GHz. Experiments in tissue simulating phantoms are used to demonstrate the feasibility of reconstructing volumetric optical properties.

2 Methods

2.1 Time-Resolved Diffuse Optical Tomography System

The design strategy for the current time-domain diffuse optical tomography (TD-DOT) system was to extend a previous fast scanning CWFT platform¹ through addition of time-resolved measurement capabilities. The system uses a planar transmission imaging geometry and provides dense spatial sampling with a large field-of-view and short scan times (Fig. 1). A pulsed source laser is raster-scanned across a “source” window and illuminates the imaging cassette. Light transmission through the imaging volume is profiled on the opposing “detector” window using a lens coupled gated image intensifier. The pulsed laser source (Becker & Hickel, BHL700, 780 nm, $T_p=100$ ps, 1 mW) provides a continuous train of light pulses (repetition rate 50 MHz). For time-resolved detection, an ultrafast image intensifier (PicoStar HR-12, LaVision, $\tau_{gate}<300$ ps) relays time-gated images of the light levels on the detection plane to an electron multiplying charged coupled device (EMCCD; iXon 877f, Andor Technologies).

With the image intensifier operating in a “comb” mode, a sequence of gated transmissions accumulates on the EMCCD during each exposure burst. The pulse train is electronically shuttered on/off with switching times <100 μ s to control the burst duration (i.e., exposure time) for each source position. The light transmitted through the tissue volume is temporally resolved by scanning the delay time (T_d) between the source laser pulse and the time-gated detection. The zero time delay, $T_d=0$, is defined as the time delay at which the instrument response function is maximum. To obtain an instrument re-

sponse function, a white sheet of paper is positioned in the imaging volume on the detector plane and a measurement set is taken. TD-DOT data sets consisted of measurements at 48 time-points (T_d from -0.5 ns to 4.2 ns in steps of 0.1 ns), with an image intensifier gate width of 0.4 ns for each source position. Temporally resolved scans are collected for each of 24 source positions, and data is extracted from the full CCD images for 24 detector positions symmetrically opposed to the source positions. The time-domain data are then converted from time-domain to frequency-domain using a Fourier transform for modulation frequencies of 208.3, 312.5, 416.7, 625, 833.3, and 1250 MHz. The frequency-domain data (Φ_i) are indexed by i , for a specified source position $r_{s(i)}$, detector position $r_{d(i)}$, and modulation frequency ω_i .

2.2 Diffuse Optical Tomography Algorithms

In this section, we detail the algorithms used to reconstruct the optical properties using light collected at the excitation wavelength. The data, Φ_i , are inverted using a first-order perturbation solution of the frequency-domain diffusion approximation.^{17,18} In the following paragraphs, we use both the diffusion coefficient ($D(\vec{r})$) and the reduced scattering coefficient $\mu'_s(\vec{r})$, which are related by the simplified expression $D(\vec{r})=\nu/3\mu'_s(\vec{r})$, where ν is the speed of light in the medium.¹⁹ The perturbation expansion separates the absorption ($\mu_a(\vec{r})$) and diffusion ($D(\vec{r})$) coefficients into background values (μ_{a0} and D_o) and spatially dependent components ($\Delta\mu_a(\vec{r})$ and $\Delta D(\vec{r})$). A scattered field, \mathbf{y} , is defined as the negative log of the ratio of Φ_i^{target} with the phantom targets over $\Phi_i^{\text{background}}$ with only background media, $y_i=-\log(\Phi_i^{\text{target}}/\Phi_i^{\text{background}})$. The scattered field is then modeled using a linear Rytov approximation, $\mathbf{y}=\mathbf{A}\mathbf{x}$, where $\mathbf{x}=[\Delta\mu_a(\vec{r})\Delta D(\vec{r})]^T=[x_a x_D]^T$ is the optical property map, and $\mathbf{A}=[W_a W_D]$, where W_a and W_D represent the sensitivity functions for the absorption and diffusion coefficients, respectively. W_a and W_s are expressed in terms of Green’s functions:

$$W_a(i,k) = -\frac{\nu h^3 G(\vec{r}_{s(i)}, \vec{r}_k, \omega_i) G(\vec{r}_k, \vec{r}_{d(i)}, \omega_i)}{D_o G(\vec{r}_{s(i)}, \vec{r}_{d(i)}, \omega_i)},$$

$$W_D(i,k) = \frac{h^3 \nabla G(\vec{r}_{s(i)}, \vec{r}_k, \omega_i) \nabla G(\vec{r}_k, \vec{r}_{d(i)}, \omega_i)}{D_o G(\vec{r}_{s(i)}, \vec{r}_{d(i)}, \omega_i)}, \quad (1)$$

where h^3 represents the voxel volume. For the current imaging geometry, the Green’s functions are slab solutions to the diffusion approximation equation.²⁰ Separating the real (R) and imaginary (I) components, the forward problem takes the following matrix form:

$$\begin{bmatrix} Y_R \\ Y_I \end{bmatrix} = \begin{bmatrix} W_{aR} & W_{DR} \\ W_{aI} & W_{DI} \end{bmatrix} \begin{bmatrix} x_a \\ x_D \end{bmatrix}. \quad (2)$$

Since the absorption x_a and diffusion x_D variables differ by orders of magnitude, preconditioning of the Jacobian matrix is necessary to reduce parameter cross talk between x_a and x_D .^{9,21,22} We precondition by normalizing the absorption and diffusion variables prior to inversion using a substitution of variables $\tilde{\mathbf{x}}=\mathbf{L}\mathbf{x}$, where

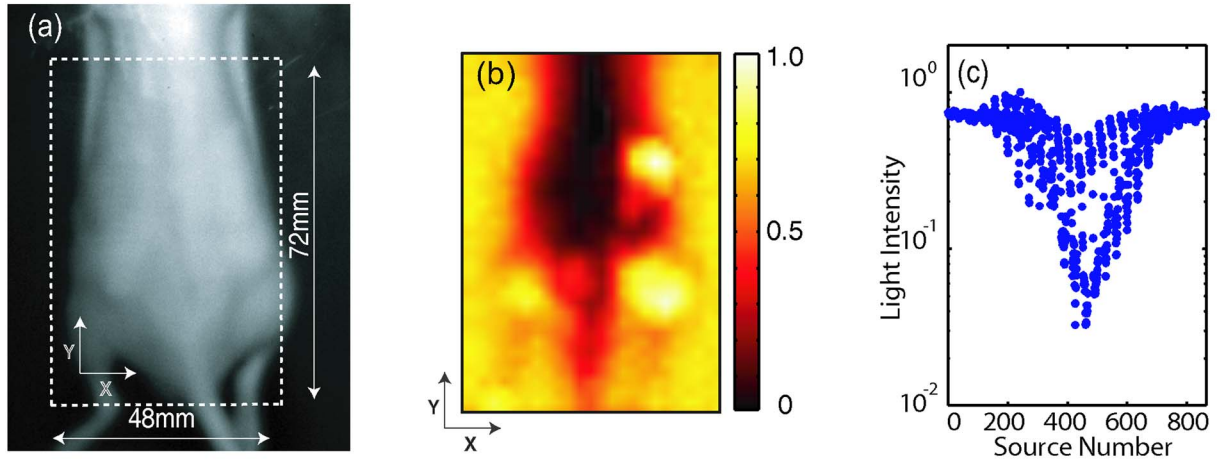


Fig. 2 Variations in the light transmitted through a mouse indicate highly heterogeneous optical properties. (a) An anaesthetized mouse was positioned in the imaging cassette, and transmission measurements were obtained at opposing source-detector pairs. (b) Map of normalized transmitted light intensity measured at the excitation wavelength. (c) A log scale plot of normalized transmitted light intensity for a listing of all the source positions shows values varying by a factor of ~ 50 .

$$\mathbf{L} = \begin{bmatrix} \|W_{aR}W_{aI}\| & 0 \\ 0 & \|W_{sR}W_{sI}\| \end{bmatrix}. \quad (3)$$

We also incorporate the measurement noise using a substitution of variables, $\tilde{y} = \mathbf{C}y$, where the diagonal of \mathbf{C} is a shot noise model. Both of these modifications are incorporated into the forward model, and we proceed with the inverse step using $\tilde{y} = \tilde{\mathbf{A}}\tilde{x}$, where $\tilde{\mathbf{A}} = \mathbf{C}\mathbf{A}\mathbf{L}^{-1}$. To stabilize the inversion, we minimize an objective function that incorporates spatially variant Tikhonov regularization:²³

$$\min \left\{ \|\tilde{y} - \tilde{\mathbf{A}}\tilde{x}\|_2^2 + \alpha \|Q\tilde{x}\|_2^2 \right\}. \quad (4)$$

The penalty term for image variance is, $\alpha \|Q\tilde{x}\|_2^2$, where α is a regularization constant, and Q is a spatially variant term where $\text{diag}(Q) = \text{sqr}[\text{diag}(\tilde{\mathbf{A}}^T\tilde{\mathbf{A}})] + \lambda$. Last, direct inversion of $\tilde{\mathbf{A}}$ is accomplished using a Moore-Penrose generalized inverse. After reconstruction, we convert maps of the diffusion coefficient to maps of the reduced scattering coefficient.

2.3 Heterogeneous Optical Properties and CW Fluorescence Tomography

To provide a context for phantom tests of our TD-DOT system, we evaluated the influence of heterogeneous optical properties on fluorescence tomography for the specific situation of small animal imaging. The distribution of effective attenuation coefficients in mice was evaluated using transmitted light measurements through mice. The TD-DOT system was reconfigured for use in the CWFT mode of operation by removing the gated image intensifier and using a continuous-wave laser diode (Hiachi, HL785G, $P_{ld} = 50$ mW, 785 nm).¹ An anaesthetized mouse was positioned in the imaging cassette. Transmission measurements (at the excitation wavelength without fluorescence emission filters) at opposing source-detector pairs were obtained over a 48 mm \times 72 mm region with 2-mm-square spacing. To provide a consistent physical path length, the tank surrounding the mouse was

filled with an optically matching solution, $\mu_a = 0.2$ cm⁻¹, and $\mu'_s = 10$ cm⁻¹, using Intralipid, water, and India ink.

In a second set of measurements, we created tissue-simulating phantoms for fluorescence tomography that matched the variation in optical properties found in the *in vivo* measurements. Three plastic tubes (3.5-mm OD) were placed in a background solution ($\mu_a = 0.1$ cm⁻¹ and $\mu'_s = 10$ cm⁻¹). Each tube had 1 μM concentration of Indocyanine Green (ICG) and each tube had variable concentrations of India ink. Emission and excitation measurements were obtained by scanning the phantom using a 12 \times 64 source-detector grid with 1-mm-square spacing. Fluorescence tomography reconstructions were performed using a homogeneous tissue model following previous procedures.¹

2.4 Evaluations of Optical Property Maps Using Tissue Simulating Phantoms

The feasibility of reconstructing absorption and scattering optical property maps using the TD-DOT system was evaluated using tissue-simulating phantoms. Tubes filled with Intralipid, water, and India ink mixture to simulate objects with increased absorption ($\mu_a = 0.44$ cm⁻¹, $\mu'_s = 15$ cm⁻¹) and increased scattering ($\mu_a = 0.12$ cm⁻¹, $\mu'_s = 40$ cm⁻¹) were used for this purpose. The tubes were suspended in the imaging cassette filled with tissue matching fluid ($\mu_a = 0.12$ cm⁻¹, $\mu'_s = 15$ cm⁻¹) and were separated by a center-to-center distance of 2 cm. Target data (with tube phantoms) and background data (without tube phantoms) were collected using the TD-DOT system in TD mode operation (Sec. 2.1).

3 Results and Discussion

3.1 The Influence of Heterogeneous Optical Properties on CW Fluorescence Tomography

The heterogeneity of the optical properties in mice is illustrated by measurements of light transmission through a mouse (Fig. 2). The influence of heterogeneous optical properties

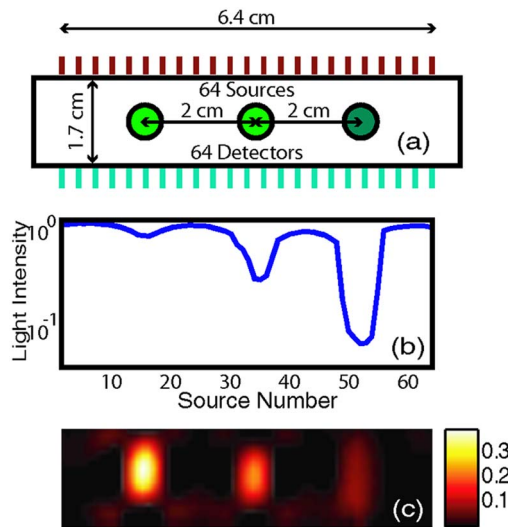


Fig. 3 Tissue-simulating phantom measurements were used to evaluate the influence of heterogeneous optical properties on fluorescence tomography. (a) Three plastic tubes were imaged. Each tube had the same 1- μ M concentration of ICG but had variable concentrations of black India ink (1 \times , 5 \times , and 10 \times more absorption than the surrounding solution $\mu_a=0.1\text{ cm}^{-1}$ and $\mu'_s=10\text{ cm}^{-1}$, left, center, and right, respectively). (b) The normalized transmitted light intensity measured at opposing source-detector pairs across the three tube phantoms. The variation in the light transmission (due to variations in India ink concentration) between the three tubes is similar to that encountered *in vivo* (Fig. 1). (c) Fluorescence tomography reconstruction of data using a homogeneous tissue model. Images of the tubes with higher absorption incorrectly indicate less fluorophore concentration.

(Fig. 2) on fluorescence tomography reconstructions is illustrated using matching tissue phantom experiments (Fig. 3).

In Fig. 2 the transmitted light intensity varies by a factor of ~ 50 (brightest to darkest) across the body of a mouse. Using $T \propto \exp(-\mu_{eff}L)$, where $L=1\text{ cm}$, and μ_{eff} is the effective attenuation coefficient, a 50-fold variation in T corresponds to a \sim fourfold variation in μ_{eff} . Since $\mu_{eff}=(3\mu_a\mu'_s)^{1/2}$, a

\sim fourfold variation in μ_{eff} corresponds to approximately a 16-fold change in either the absorption or the reduced scattering coefficients.

The influence of this degree of heterogeneity on fluorescence tomography reconstructions was evaluated using tissue-simulating phantoms. Three tubes had identical fluorophore concentrations (1 μ M ICG) and variable amounts of India ink so that the tubes left, center, and right had absorption coefficients 1 \times , 5 \times , and 10 \times the background, respectively (Fig. 3). Reconstructions using a homogeneous tissue mode produce images with values that incorrectly vary by up to a factor of 5. In such situations, *in situ* optical property maps are needed to correctly reconstruct fluorophore distributions.

3.2 Evaluations of TD-DOT Optical Property Maps

Figure 4 illustrates the concept of time-resolved measurements where the pulsed laser illuminates the imaging cassette and the gated intensifier time-resolves light emitted from the opposing window. Due to scattering and absorption, the detected pulse has decreased intensity and is delayed; its dependence on source-detector separation is also illustrated. Figure 4(a) shows the system response function with time $t=0\text{ s}$ along with the response to a homogeneous medium as measured by three equally spaced detectors with increasing source-detector separation. The signal amplitude falls off exponentially with increasing source-detector separation, while the mean time-of-flight increases with distance, reflecting an increase in mean path length with increased source-detector distance. The data were converted using a Fourier transform from time-domain to frequency-domain. The signal amplitude [Fig. 4(b)] and phase [Fig. 4(c)] at three representative modulation frequencies: 312.5 MHz (blue), 625 MHz (green), and 1250 MHz (red), are shown for the middle (12th) source and all the detectors. (Color online only).

The utility of frequency domain data for distinguishing between absorbing and scattering objects can be observed directly in the measurement data. Two tubes with diameter 5 mm were imaged, one with increased absorption

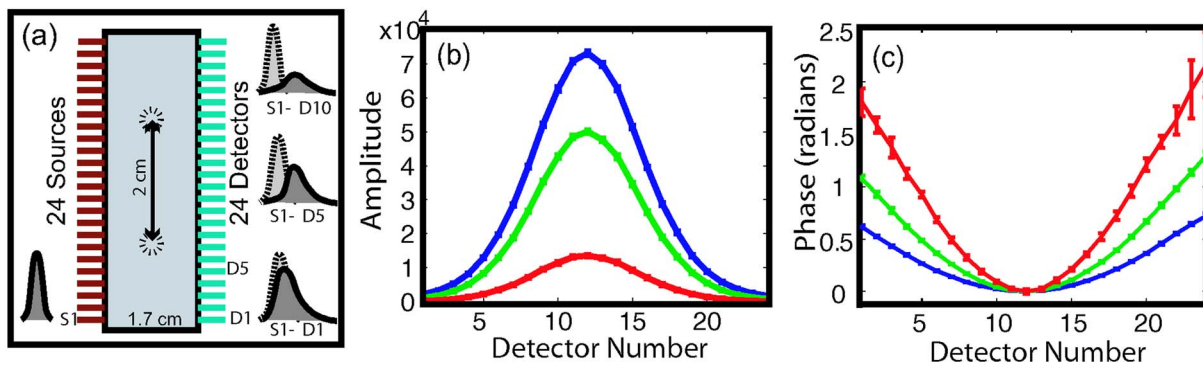


Fig. 4 Measurement setup and conversion of time-resolved measurements to frequency domain data using Fourier transform. (a) The concept of time-domain measurement is illustrated—the input laser pulse is delayed and broadened when sampled on the detector window. Two phantom targets are placed at the center of the imaging cassette and scanned using 24 source and 24 detector positions. The signal amplitude (b) and phase (c) for three modulation frequencies, 312.5 MHz (blue, top curve for amplitude and bottom curve for phase), 625 MHz (green), and 1250 MHz (red), are calculated by Fourier transform of the time-domain measurements (data shown for the 12th source and all the detectors), phase values are relative to the phase for detector 12. (Color online only)

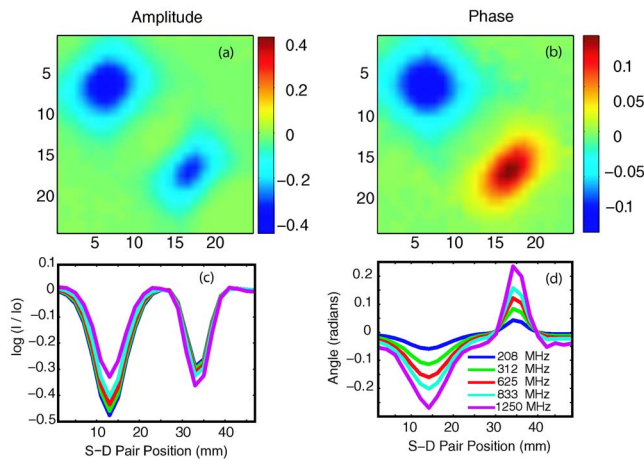


Fig. 5 Frequency domain data: (a) amplitude and (b) phase of the noise-weighted differential measurements using a 625-MHz modulation frequency where each pixel represents a source-detector pair. The absorbing object (upper left) has decreased amplitude and a negative phase delay, while the scattering object (lower right) has decreased amplitude with a positive phase delay. The diagonal values represent opposing source-detector pair measurements, which are shown in (c) and (d) for modulation frequencies from 208 MHz to 1.25 GHz. It can be observed that lower modulation frequencies provide better amplitude contrast while higher modulation frequencies provide better phase contrast.

($\mu_a=0.44 \text{ cm}^{-1}$, $\mu'_s=15 \text{ cm}^{-1}$), and one with increased scattering ($\mu_a=0.12 \text{ cm}^{-1}$, $\mu'_s=40 \text{ cm}^{-1}$). Differential data, y , is weighted by the signal-to-noise ratio (SNR) of the light intensity measurements using a noise value proportional to the square root of the intensity. In Fig. 5, the noise-weighted differential amplitude and phase measurements for a modulation frequency of 625 MHz are depicted as images in which each pixel represents a source-detector pair. The amplitude of the scattered wave is negative for both the scattering and absorbing objects while the phase shows an increased delay for the scattering object (lower right) and decreased delay for the absorbing object (upper left). The diagonal elements of these images, which represent opposing source-detector pair measurements, are shown in Figs. 5(c) and 5(d) for modulation frequencies from 208 MHz to 1.25 GHz. Significant contrast is evident for both the scattering and the absorbing objects for all modulation frequencies.

Figures 6(a) and 6(b) show the peak contrast in amplitude and phase for the absorption (red) and scattering (blue) objects as a function of modulation frequency. The error bars indicate standard deviation in 10 independent measurements. The amplitude contrast for the scattering object increases, while that for the absorbing object decreases with the modulation frequency. The phase contrast, on the other hand, increases with modulation frequency for both the scattering and the absorbing object. Excellent contrast and noise are obtained for modulation frequencies up to 1 GHz. At higher frequencies, the noise begins to grow significantly.

In Fig. 7, reconstructions of the absorption (a) and scattering (b) perturbations demonstrate the capability to separate the two optical properties using data at 625-MHz modulation frequency. In order to check the quantitative accuracy of the reconstructions, we compared volume-integrated

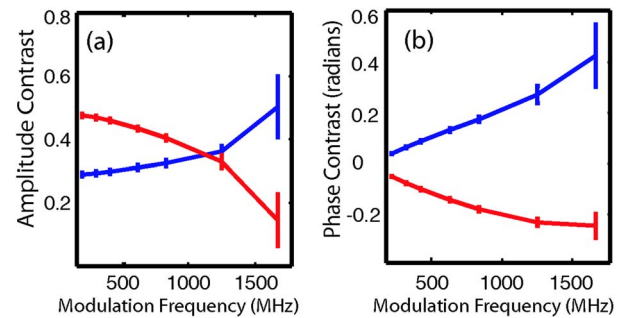


Fig. 6 The differential contrasts in (a) amplitude and (b) phase as a function of modulation frequency. The peak values in the amplitude and phase measurements corresponding to the absorption (red) and scattering (blue) object are plotted, with error bars indicating the standard deviation in 10 independent measurements.

signals normalized by the phantom tube volume V_T (or normalized volume integrated (NVI) signals) for the expected $NVI_e = \int S_{expected} dv / V_T$ and reconstructed $NVI_r = \int S_{reconstruction} dv / V_T$ images, where S is the signal value in a voxel. The region of interest surrounding the tube phantoms is used in calculating NVI_r . The expected values for NVI_e are 0.32 cm^{-1} ($\Delta\mu_a$) and 25 cm^{-1} ($\Delta\mu'_s$). The reconstructed NVI_r values are 0.34 cm^{-1} ($\Delta\mu_a$) and 22.58 cm^{-1} ($\Delta\mu'_s$), both within an error $<10\%$ with respect to the NVI_e .

To provide a more comprehensive evaluation, we also tested two other situations: the ability of the system to reconstruct phantoms with both absorption and scattering perturbations, and the ability to image over a range of contrasts. For the first imaging task, we reconstructed three tubes (diam=3 mm), one with only absorption contrast ($\mu_a=0.44 \text{ cm}^{-1}$, $\mu'_s=15 \text{ cm}^{-1}$), one with both absorption and scattering ($\mu_a=0.44 \text{ cm}^{-1}$, $\mu'_s=40 \text{ cm}^{-1}$), and one with only a scattering contrast ($\mu_a=0.12 \text{ cm}^{-1}$, $\mu'_s=40 \text{ cm}^{-1}$) as shown in Figs. 8(a) to 8(c). In the reconstructed images [Figs. 8(b) and 8(c)], each tube shows up with the appropriate combinations of contrast with minimal cross talk between absorption and scattering. For the second imaging task, we varied the absorption coefficient [Fig. 8(d), $\mu_a=0.44 \text{ cm}^{-1}$, 0.34 cm^{-1} ,

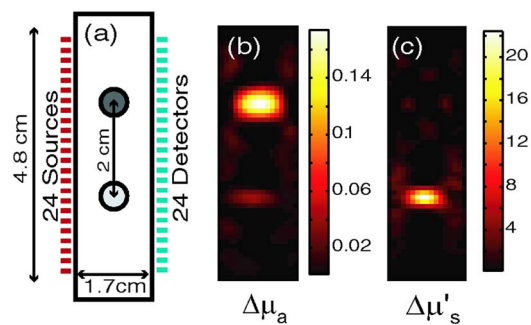


Fig. 7 (a) Frequency domain phantom data at 625-MHz modulation frequency were obtained with both an absorbing and a scattering tube (diameter 5 mm). Reconstructed slices of (b) absorption and (c) scattering components show a clear separation of the two objects. The volume average values of contrast are in agreement with the expected values within 10% (see text).

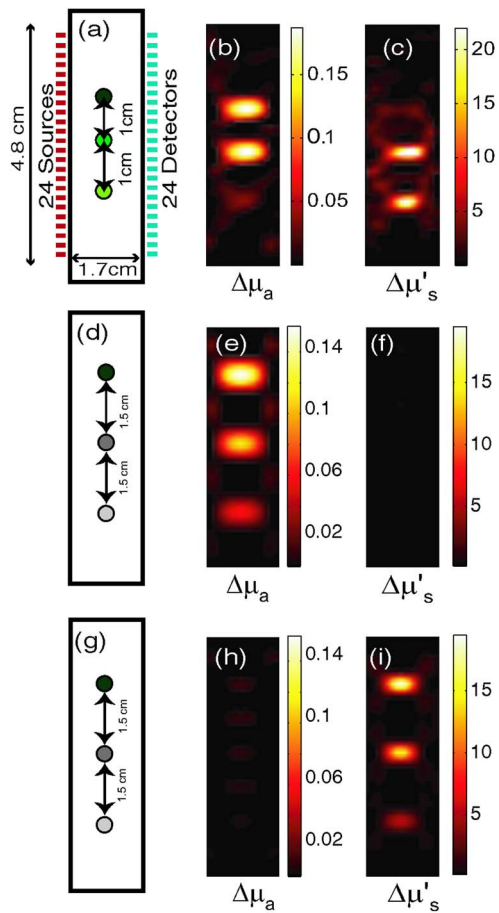


Fig. 8 Evaluations of mixed scattering and absorption contrast phantoms. (a) Mixed contrast targets were evaluated using three tubes (diameter 3 mm): top tube—only μ_a 3.7:1; center tube—both μ_a 3.7:1 and μ'_s 2.7:1; bottom tube— μ'_s 2.7:1. All values expressed as a ratio to background optical properties ($\mu_a=0.12 \text{ cm}^{-1}$, $\mu'_s=15 \text{ cm}^{-1}$). (b) Absorption coefficient reconstruction. (c) Reduced scattering coefficient reconstruction. (d) to (f) Three tubes were programmed for titrations of μ_a while holding μ'_s fixed. (g) to (i) Three tubes were programmed for titrations of μ'_s while holding μ_a fixed.

and 0.24 cm^{-1} , top to bottom, respectively] while holding the reduced scattering coefficient constant and then varied the reduced scattering coefficient while holding the absorption constant [Fig. 8(g), $\mu'_s=20 \text{ cm}^{-1}$, 30 cm^{-1} , and 40 cm^{-1} , top to bottom, respectively]. The reconstructions performed as expected for both the absorption titration [Figs. 8(e) and 8(f)] and the reduced scattering titration [Figs. 8(h) and 8(i)]. Targets showed graded contrasts and minimal cross talk between the absorption and reduced scattering coefficients.

Using single modulation frequency measurements in the reconstruction, the interparameter cross talk is less than 10%. Similar reconstructions were obtained for 208.3, 312.5, 416.7, 833.3, and 1250 MHz modulation frequency data sets. The resolution of the scattering object [e.g., full width half maximum (FWHM)] is better than the resolution for the absorbing object at all modulation frequencies. This is in agreement with previous theoretical and experimental results.²⁴

The interaction between modulation frequency and optical properties and their combined effect on image quality for

single-frequency data sets has been examined. O'Leary et al. found in simulation studies that when background absorption is high ($\mu_a=1 \text{ cm}^{-1}$), an increase in modulation frequency from 50 MHz to 1 GHz has no effect on image quality.¹⁷ However, for low absorption ($0.01 < \mu_a < 0.1 \text{ cm}^{-1}$), image quality improved. Jiang et al.,²⁵ using both simulated and measured data, found minimal effect of modulation frequency on reconstructions.

Reconstructions that combine measurements at several frequencies are expected to reduce the interparameter cross talk, provide better resolution, and increase the measurement information content. Intes et al.²¹ have reported simulation studies with modulation frequencies from 20 to 500 MHz where different preconditioning techniques of the weight matrix were compared for image quality and cross talk. Their results indicate that increasing the number of frequencies gave a decrease in interparameter cross talk and the column scaling preconditioning scheme resulted in less cross talk and better estimates. Gulsen et al.²⁶ have compared multiple-frequency reconstruction with reconstructions from various individual frequencies. Multifrequency images had lowest measurement error and highest contrast-to-noise ratio (CNR), and also the noise near the source-detector positions was reduced. Future studies with more complex phantoms and a range of object contrasts are needed to evaluate and optimize the effects of modulation frequency and multiple-frequency reconstructions for our system.

4 Conclusions

The data presented demonstrate the feasibility of reconstructing the three-dimensional (3-D) optical property maps of small tissue volumes relevant for imaging mice from high-frequency time-resolved amplitude and phase measurement. Useful CNRs were obtained even for modulation frequencies in the range of 300 to 1250 MHz, and absorption and scattering components were successfully reconstructed and separated. The *in situ* heterogeneous optical property maps obtained with this diffuse optical tomography system can be used as a basis for quantitative fluorescence or bioluminescence^{1,2,27} tomography of small animals. In this paper, we reconstructed optical properties at a single wavelength. A more complete assessment, with mapping of the optical properties at both the excitation and emission wavelengths for a given fluorophore, could be achieved through a straightforward extension of the current system to a two or more wavelength system. Use of an ICCD permits integration of this approach into our existing CW small animal fluorescence tomography system. Compared to fluorescence reconstructions using homogeneous tissue models, volumetric images obtained using heterogeneous tissue models are expected to provide a more uniform mapping of fluorophore concentration and activity independent of local or nearby tissue optical properties.²⁸ We anticipate that as fluorescence tomography becomes more widely used, the development of methods to measure and incorporate heterogeneous optical property maps into fluorescence tomography reconstructions will become increasingly important.

Acknowledgments

The authors acknowledge useful discussions with Samuel Achilefu and the help of Walter Akers for animal preparation. This work was supported in part by the following research grants: National Institutes of Health Grant Nos. K25-NS44339 and BRG R01 CA109754 and Small Animal Imaging Resource Program (SAIRP) Grant No. R24 CA83060.

References

1. S. V. Patwardhan, S. R. Bloch, S. Achilefu, and J. P. Culver, "Time-dependent whole-body fluorescence tomography of probe bio-distributions in mice," *Opt. Express* **13**(7), 2564–2577 (2005).
2. V. Ntziachristos, C. H. Tung, C. Bremer, and R. Weissleder, "Fluorescence molecular tomography resolves protease activity *in vivo*," *Nat. Med.* **8**(7), 757–760 (2002).
3. V. Ntziachristos and R. Weissleder, "Experimental three-dimensional fluorescence reconstruction of diffuse media by use of a normalized Born approximation," *Opt. Lett.* **26**(12), 893–895 (2001).
4. A. Soubret, J. Ripoll, and V. Ntziachristos, "Accuracy of fluorescent tomography in the presence of heterogeneities: study of the normalized Born ratio," *IEEE Trans. Med. Imaging* **24**(10), 1377–1386 (2005).
5. M. J. Eppstein, D. E. Dougherty, D. J. Hawrysz, and E. M. Sevick-Muraca, "Three-dimensional Bayesian optical image reconstruction with domain decomposition," *IEEE Trans. Med. Imaging* **20**(3), 147–163 (2001).
6. A. P. Gibson, J. C. Hebden, J. Riley, N. Everdell, M. Schweiger, S. R. Arridge, and D. T. Delpy, "Linear and nonlinear reconstruction for optical tomography of phantoms with nonscattering regions," *Appl. Opt.* **44**(19), 3925–3926 (2005).
7. X. F. Cheng and D. A. Boas, "Systematic diffuse optical image errors resulting from uncertainty in the background optical properties," *Opt. Express* **4**(8), 299–307 (1999).
8. S. R. Arridge and W. R. B. Lionheart, "Nonuniqueness in diffusion-based optical tomography," *Opt. Lett.* **23**(11), 882–884 (1998).
9. T. O. McBride, B. W. Pogue, S. Jiang, U. L. Osterberg, and K. D. Paulsen, "A parallel-detection frequency-domain near-infrared tomography system for hemoglobin imaging of the breast *in vivo*," *Rev. Sci. Instrum.* **72**(3), 1817–1824 (2001).
10. F. E. W. Schmidt, M. E. Fry, E. M. C. Hillman, J. C. Hebden, and D. T. Delpy, "A 32-channel time-resolved instrument for medical optical tomography," *Rev. Sci. Instrum.* **71**(1), 256–265 (2000).
11. V. Ntziachristos, X. H. Ma, A. G. Yodh, and B. Chance, "Multichannel photon counting instrument for spatially resolved near infrared spectroscopy," *Rev. Sci. Instrum.* **70**(1), 193–201 (1999).
12. A. B. Thompson and E. M. Sevick-Muraca, "Near-infrared fluorescence contrast-enhanced imaging with intensified charge-coupled device homodyne detection: measurement precision and accuracy," *J. Biomed. Opt.* **8**(1), 111–120 (2003).
13. J. Selb, M. A. Franceschini, A. G. Sorensen, and D. A. Boas, "Improved sensitivity to cerebral hemodynamics during brain activation with a time-gated optical system: analytical model and experimental validation," *J. Biomed. Opt.* **10**(1), 011013 (2005).
14. G. M. Turner, G. Zacharakis, A. Soubret, J. Ripoll, and V. Ntziachristos, "Complete-angle projection diffuse optical tomography by use of early photons," *Opt. Lett.* **30**(4), 409–411 (2005).
15. V. Ntziachristos, J. P. Culver, M. Holboke, A. Yodh, and B. Chance, "Optimal selection of frequencies for diffuse optical tomography," in *Biomedical Topical Meetings*, OSA, Miami Beach, Florida (2001).
16. B. J. Tromberg, L. O. Svaasand, T. T. Tsay, and R. C. Haskell, "Properties of photon density waves in multiple-scattering media," *Appl. Opt.* **32**(4), 607–616 (1993).
17. M. A. O'Leary, D. A. Boas, B. Chance, and A. G. Yodh, "Experimental images of heterogeneous turbid media by frequency-domain diffusing-photon tomography," *Opt. Lett.* **20**(5), 426–428 (1995).
18. V. Ntziachristos, B. Chance, and A. G. Yodh, "Differential diffuse optical tomography," *Opt. Express* **5**(10), 230–242 (1999).
19. T. Durduran, A. G. Yodh, B. Chance, and D. A. Boas, "Does the photon-diffusion coefficient depend on absorption?," *J. Opt. Soc. Am. A* **14**(12), 3358–3365 (1997).
20. M. S. Patterson, B. Chance, and B. C. Wilson, "Time-resolved reflectance and transmittance for the non-invasive measurement of tissue optical properties," *Appl. Opt.* **28**, 2331–2336 (1989).
21. X. Intes and B. Chance, "Multi-frequency diffuse optical tomography," *J. Mod. Opt.* **52**(15), 2139–2159 (2005).
22. Y. L. Pei, H. L. Graber, and R. L. Barbour, "Normalized-constraint algorithm for minimizing inter-parameter crosstalk in DC optical tomography," *Opt. Express* **9**(2), 97–109 (2001).
23. J. P. Culver, T. Durduran, D. Furuya, C. Cheung, J. H. Greenberg, and A. G. Yodh, "Diffuse optical tomography of cerebral blood flow, oxygenation and metabolism in rat during focal ischemia," *J. Cereb. Blood Flow Metab.* **23**, 911–923 (2003).
24. J. C. Hebden and S. R. Arridge, "Imaging through scattering media by the use of an analytical model of perturbation amplitudes in the time domain," *Appl. Opt.* **35**(34), 6788–6796 (1996).
25. H. B. Jiang, K. D. Paulsen, U. L. Osterberg, B. W. Pogue, and M. S. Patterson, "Optical image reconstruction using frequency-domain data: simulations and experiments," *J. Opt. Soc. Am. A* **13**(2), 253–266 (1996).
26. G. Gulsen, B. Xiong, O. Birgul, and O. Nalcioglu, "Design and implementation of a multifrequency near-infrared diffuse optical tomography system," *J. Biomed. Opt.* **11**(1), 014020-1-10 (2006).
27. H. Dehghani, S. C. Davis, S. D. Jiang, B. W. Pogue, K. D. Paulsen, and M. S. Patterson, "Spectrally resolved bioluminescence optical tomography," *Opt. Lett.* **31**(3), 365–367 (2006).
28. S. Bjoern, S. V. Patwardhan, and J. P. Culver, "The influence of heterogeneous optical properties on fluorescence diffusion tomography of small animals," in *Optical Society of America Biomedical Optics Conference*, Florida (2006).